Pulsatile Cerebrospinal Fluid Dynamics in the Human Brain

Andreas A. Linninger*, Cristian Tsakiris, David C. Zhu, Michalis Xenos, Peter Roycewicz, Zachary Danziger, and Richard Penn

***Abstract*—Disturbances of the cerebrospinal fluid (CSF) flow in the brain can lead to hydrocephalus, a condition affecting thousands of people annually in the US. Considerable controversy exists about fluid and pressure dynamics, and about how the brain responds to changes in flow patterns and compression in hydrocephalus. This paper presents a new model based on the first principles of fluid mechanics. This model of fluid-structure interactions predicts flows and pressures throughout the brain's ventricular pathways consistent with both animal intracranial pressure (ICP) measurements and human CINE phase-contrast magnetic resonance imaging data. The computations provide approximations of the tissue deformations of the brain parenchyma. The model also quantifies the pulsatile CSF motion including flow reversal in the aqueduct as well as the changes in ICPs due to brain tissue compression. It does not require the existence of large transmural pressure differences as the force for ventricular expansion. Finally, the new model gives an explanation of communicating hydrocephalus and the phenomenon of asymmetric hydrocephalus.**

***Index Terms*—CSF flow, fluid-structure interactions, hydrocephalus, intracranial pressure, tissue compliance.**

NOMENCLATURE

A_i	Cross section of the ventricular or subarachnoid section [m^2].
$a(t)$	Choroid plexus displacement [m].
h_i	Height of the ventricular or subarachnoid section [m].
k_e	Tissue elasticity constant [N/m].
k_d	Tissue compliance [(N s)/m].
F_i	Poiseuille Friction term [N/m^3].
l_i	Length of foramina connecting ventricles [m].
$p_0(t)$	Pressure of brain parenchyma [N/m^2].
$p_i(t), p_{\mathrm{SAS}}(t)$	CSF pressure in ventricles and subarachnoid section—ICP [N/m^2].
$q_{e,j}(t)$	Reabsorption flow rate in a section [m^3/s].
$q_{f,i}(t)$	CSF production rate in the choroid plexus [m^3/s].
$q_i(t) = A_i v_i$	CSF flow rate leaving ventricle, i.e., flow in formina and aqueduct [m^3/s].
r_i	Radius of the foramina and aqueduct [m].
$v_i(t)$	Axial CSF flow velocity [m/s].
$y_i(t)$	Tissue displacement in a section [m].

Greek Symbols

α	Amplitude of choroid expansion [m].
δ	Tissue width [m].
κ	Reabsorption constant [m^3/(Pa s)].
μ	Fluid Viscosity [Pa s].
ρ	Fluid density [kg/m^3].
ρ_w	Tissue density [kg/m^3].
ω	Heart rate frequency [rad/s].

Manuscript received March 12, 2004; revised August 29, 2004. *Asterisk indicates corresponding author.*

*A. A. Linninger is with the Laboratory for Product and Process Design (LPPD), Department of Chemical Engineering, University of Illinois at Chicago 810 S. Clinton Street, CEB 216, Chicago, IL 60607 USA (e-mail: linninge@uic.edu).

C. Tsakiris, M. Xenos, P. Roycewicz, and Z. Danziger are with the Laboratory for Product and Process Design (LPPD), Department of Chemical Engineering, University of Illinois at Chicago, Chicago, IL 60607 USA.

D. C. Zhu is with the Department of Radiology, University of Chicago, Chicago, IL 60607 USA.

R. Penn is with the Department of Neurosurgery, University of Chicago, Chicago, IL 60607 USA.

Digital Object Identifier 10.1109/TBME.2005.844021

I. INTRODUCTION

IN 1976, Hakim [1] proposed an important model of the brain as a sponge, postulating that large transmural pressure differences between the SAS and ventricles cause ventricular enlargement by squeezing water out of the brain parenchyma. While this may occur in obstructive hydrocephalus in which a tumor or injury blocks the proximal CSF pathways, large pressure gradients predicted by Hakim are not consistent with the open foramina in communicating hydrocephalus. Furthermore, Hakim's hypothesis cannot explain why the intracranial pressure (ICP) often returns to almost normal levels in patients with communicating hydrocephalus.

An understanding of the basic underlying fluid mechanics in the normal brain and in hydrocephalus is needed to develop more effective medical treatments. In particular, the pulsatile flow rates, ICPs, pressure gradients, and their interaction with each other need to be understood in order to design CSF shunting systems which compensate correctly for the fluid dynamic abnormalities.

This paper presents a comprehensive computational model of normal and hydrocephalic CSF flow. The first section reviews experiments on dogs that show CSF flow is pulsatile and large pressure gradients are not present. The second section proposes a mathematical model of intracranial dynamics based on first principles of fluid mechanics. The third section presents simulation results for normal CSF flow and demonstrates conditions leading to hydrocephalus. The validation section provides experimental evidence to support the proposed mechanisms, and validates the simplified assumptions of using two-dimensional

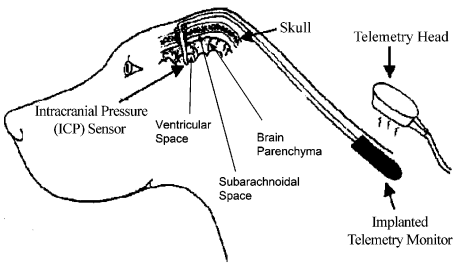

Fig. 1. Placement of ICP monitors in dog experiments. (Only one monitor is shown for clarity.).

(2-D) computational fluid dynamic (CFD) simulations. The simulations are also compared with data from CINE phase-contrast magnetic resonance imaging (MRI).

II. Animal Experiments

A series of experiments on dogs was performed to establish the role of ICP gradients in communicating hydrocephalus. Multiple INSITE pressure sensors (Medtronic, Inc., Minneapolis, MN) were implanted for simultaneous *in vivo* measurements. This new technique generated both long-term and real-time ICP measurements. The sensors were placed in three different locations: the lateral ventricle, the brain parenchyma, and the SAS as shown in Fig. 1. Real-time measurements were obtained at 256 ICP data points per second. Long-term ICP trends were recorded for a period of 20 days with the average pressure sampled every 5 min. A more detailed description of the experiments is given elsewhere [2].

Six dogs were injected cisternally with kaolin to induce hydrocephalus. In one dog, the ICP rose rapidly both in the absolute value and in the pulse pressure, peaking at about 10 000 Pa (∼70 Torr) above normal (Fig. 2). The huge ICP rise was fatal to this dog within 16 h. The autopsy of the animal showed expanded ventricles consistent with acute communicating hydrocephalus. The SAS was found to be clogged with kaolin. In effect, kaolin injection blocked the CSF reabsorption through the SAS. This dog's ventricular expansion appears to be a consequence of CSF accumulation. The duration for reaching the peak ICP is consistent with CSF accumulation at constant production, with minimal reabsorption [3], [4].

In four dogs, chronic hydrocephalus was induced. Both the long-term and real-time data from simultaneous recordings failed to show any measurable pressure gradients across the ventricle to the parenchyma or the SAS to the parenchyma (Fig. 3). Autopsy confirmed moderate hydrocephalus in all four dogs. One dog did not develop chronic hydrocephalus, and died with seizures after a second kaolin injection.

The experimental data show that the ICP is pulsatile with a peak in systole and a valley in diastole. The synchronization of CSF pressure with the cardiac cycle corroborates the clinical evidence linking CSF motion in the ventricular system to arterial pulsations. Recently, Egnor [5] has proposed that pulsatile choroid plexus motion due to arterial pulsations actively powers the CSF's oscillatory motion in the ventricles.

In Hakim's hypothesis, transmural pressure gradients across the parenchyma are essential for explaining ventricular expansion [1]. However, in our experiment such large pressure differences were not found. In fact, no transmural pressure differences in our dogs were seen, see Fig. 3. If pressure differences do exist, they are below 1–2 Torr (133–267 Pa), the sensitivity of the ICP monitors. Our first principles analysis in the next section will provide an explanation why large transmural pressure differences cannot develop with open ventricular pathways.

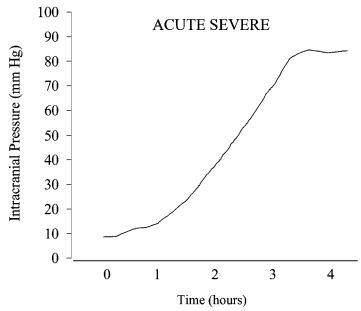

Fig. 2. Experimental ICP increments measured in an acutely hydrocephalic dog. (Pulse pressure not shown in this chronic record.).

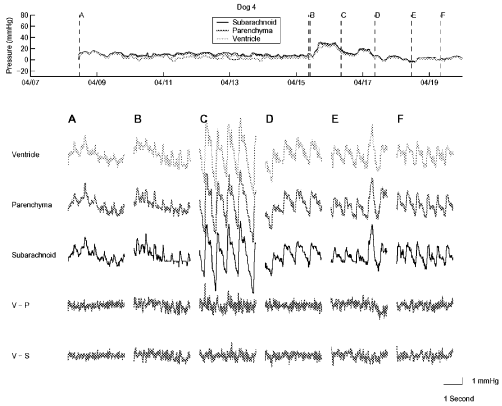

Fig. 3. Long-term ICP chronic hydrocephalic dog and real-time pressure difference between ventricles and parenchyma (V-P) and ventricles and SAS (V-S). The top graph shows chronic recordings prior to kaolin injection (up to B) and then after as the ICP elevates and returns to normal with the development of hydrocephalus. The middle three records are the real-time pressure of the ventricle, parenchyma and SAS. The lower two are subtractions of ventricle minus parenchmyma pressure (V-P) and ventricle minus SAS pressure (V-S). No significant pressure gradient is observed.

III. Modeling of the CSF Dynamics

CSF oscillatory flow results from cardiac pulsations ([1], [5]–[7]). The pattern and timing of CSF motion has been studied extensively with MRI techniques ([6]–[9]). Nevertheless, the causes and mechanical principles underlying intracranial dynamics are controversial. Some authors link the CSF flow to the brain motion. This hypothesis is supported by careful measurements of brain motion using CINE phase-contrast MRI, [9]–[11]. Other investigators suggest a pulsatory thalamic pump actively pushing the CSF [12]. A competing view attributes CSF motion to a transmission of the arterial pressure in the choroid plexus. Another study, which combined gated MR with automated edge-detection algorithms, observed a 10%–20% variation in size of the lateral ventricles during the normal cardiac cycle [13]. These measurements are not consistent with the brain motion hypothesis according to which arterial pulsation should diminish the ventricular size in the systole.

The critical role of the choroid plexus in the development of communicating hydrocephalus was established by Bering [14]. In dogs injected with kaolin, he found that only ventricles with an intact choroid plexus expanded. If the choroid plexus had been removed, the ventricle did not enlarge. Thus, the choroid plexus is necessary for ventricular expansion in communicating hydrocephalus.

All these phenomena, including arterial expansion, brain motion and choroid expansion are likely to contribute to some extent. In order to understand intracranial dynamics better, a mathematical model quantifying forces and their interaction is needed to evaluate the different hypotheses. This section introduces a model based on the first principles of fluid mechanics which is designed to calculate stresses, strains and displacement in the cranial cavity. We made the choroid plexus as the principal driver of CSF motion. The effects of complex brain motion resulting from cardiac pulsations transmitted to the intracranial space [9] are not difficult to incorporate into our bio-mechanical model.

The first principles model for pulsatile CSF flow relates three dynamically interacting systems: the cerebral vascular system, the CSF-filled ventricular and SAS, and the brain parenchyma. Fig. 4 illustrates how the CSF pulsatile motion in the ventricular system occurs in our view. Arterial blood flows into the distensible tissues of the choroid plexus cause it to expand during systole. Simultaneously, new CSF is produced in the choroid plexus by secretion at a constant rate ([14]–[18]). Thus, the choroid plexus acts like a pump, and drives the pulsatile CSF circulation. The transient velocities and pressure field in turn lead to periodic compression of the brain parenchyma observable as ventricular pulsations.

Fig. 5 is a schematic of the CSF pathways interacting with the vascular system and the parenchyma. The CSF traverses the lateral ventricles (V1 and V2), the foramina of Monro (FM), the third ventricle (V3), and flows into the fourth ventricle (V4) through the aqueduct of Sylvius (AS), and then finally reaches the subarachnoid space (SAS) through the foramina of Luschke (FL) and Magendie (FMa). In the SAS, CSF is reabsorbed into the sagittal sinus along the top of the cranium and also in the spinal canal. The pulsatile CSF motion is effectively powered by the kinetic energy of the arterial pump of the choroid plexus. The expansion and compression of the parenchyma influences the blood perfusion and, thus, provides a feedback loop on the CSF dynamics [19].

The goal of our detailed hydrodynamic modeling is to compute the CSF pressure and velocity fields throughout the brain for comparison with clinical data. The fluid motion obeys the continuity and the Navier–Stokes equations. The dynamics of parenchyma stresses, strains and displacements can be described with the laws of elastodynamics. At the interface of the fluid and the elastic tissue, the boundary conditions dictate equality of displacements and stresses. Since the deformation of the tissues directly affects the space available to the fluid, the two systems are fully coupled. Instead of directly resolving the complex three-dimensional (3-D) dynamic brain deformation problem with fluid-structure interaction, a few assumptions are taken to simplify the mathematics. Theses assumptions will be justified in the validation section by means of a commercial CFD tool [20].

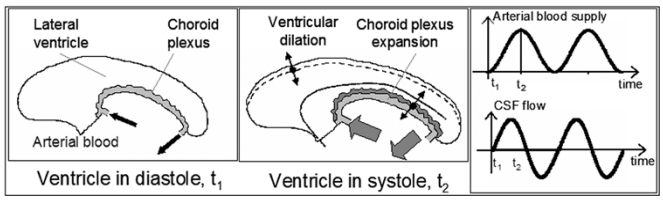

Fig. 4. CSF flow due to the choroid plexus.

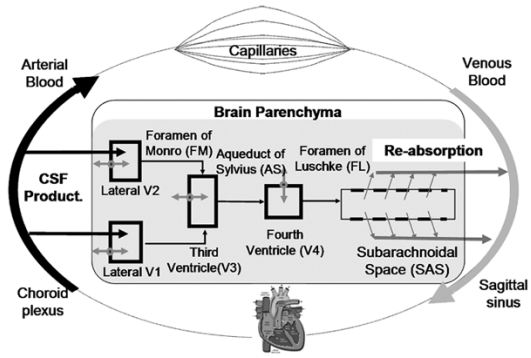

Fig. 5. Schematic of CSF pathways, the vascular system and brain parenchyma.

The initial mathematical framework for one-dimensional (1-D) intracranial dynamics is as follows. The forces and displacements for each ventricle interacting with the elastic brain tissues are depicted in Fig. 6. A difference in fluid (p_i) and intracranial tissue pressure (p_0) causes the extension of the ventricular wall. In this first approach, only a thin layer of epithelial cells in the peri-ventricular area is included. This simplification allows adopting the standard thin elastic membrane model of tissue deformation [21]. The acceleration of a small membrane segment results from the interaction of three forces: the difference between fluid and tissue pressures $(p_i - p_0)$, the tissue elasticity $(k_e \cdot y_i)$ as well as a dissipative force $(k_d \cdot \dot{y}_i)$. The interior of the ventricle is compressed by the choroid plexus. The cyclic motion of choroid plexus follows the cardiac cycle and is represented by the forcing function $a(t)$ given in (1)

$$a(t) = \alpha \left(1.3 + \sin\left(\omega t - \frac{\pi}{2}\right) - \frac{1}{2}\cos\left(2\omega t - \frac{\pi}{2}\right)\right). \quad (1)$$

In ensemble, the relative dynamics of choroid expansion $a(t)$ and the induced tissue expansion $y_i(t)$ determine the instantaneous CSF content in the ventricle as well as the CSF flow rate along the proximal pathways at each instant of time. To resolve the ventricular dynamics better, the ventricles were also discretized into cylindrical finite volumes with perfect axial dispersion and radial expandability against the thin periventricular membrane [22], see Fig. 6. The foramina are treated as elastic tubes. Since the diameters of all foramina are small, averaged axial velocities (v_i) were considered in the momentum balances. The radial CSF momentum balance in the thin foramina was neglected. The radial velocity components equal to the tissue deformation speed $\dot{y}_i$ appear in the continuity

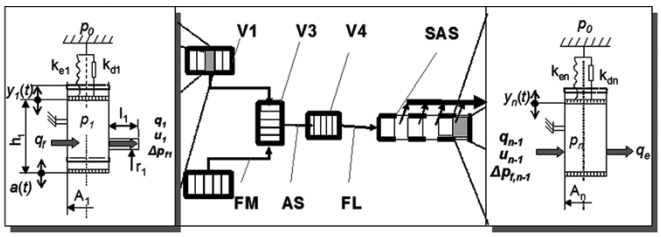

Fig. 6. The discretized model of CSF flow induced by choroid expansion $a(t)$.

as an apparent volume change, cf. $A\dot{y}_i(t)$. Since the CSF flow is basically laminar based on its very low Reynolds numbers ($\mathrm{Re} < 100$, [23]), the flow friction was expressed as a function of the cross-sectional area. The Poiseuille term (F) is strictly valid only for steady flow, but is used as a first approximation widely applied in hydrodynamic studies [24].

The SAS is the location where CSF is reabsorbed through the arachnoid villi at the sagittal sinus into the venous system. The reabsorption is discretized into porous finite volumes. The mass transfer is diffusive and is driven by the pressure difference between the SAS and the venous pressure of the sagittal sinus. The CSF pressure is normally higher than the venous pressure, and the villi act as one-way valves. The geometry with the proposed simplifications and discretization techniques is depicted schematically in Fig. 6.

The equation for the acceleration of the elastic tissue is

$$(\rho_w A_i \delta)\ddot{y}_i(t) + k_d\dot{y}_i(t) + k_e y_i(t) - A_i[p_i(t) - p_0(t)] = 0, \quad i \in \{LV_1 - LV_4, \mathrm{SAS}\}. \quad (2)$$

The continuity of the CSF flow in the ventricles is given by

$$\frac{\partial\{A_i[h_i + a(t) + y_i(t)]\}}{\partial t} = q_{f,i} - q_i, \quad i \in \{LV_1 - LV_4\}. \quad (3)$$

The axial momentum equation along a streamline in the flow direction is valid in foramina and is given by

$$\rho\left[\frac{\partial v_i}{\partial t} + v_i\frac{\partial v_i}{\partial z}\right] + \frac{\partial p_i(t)}{\partial z} = -F_i, \quad i \in \{FM, AS, FL\} \quad \text{with } F_i = \frac{8\mu}{r_i^2}v_i. \quad (4)$$

The continuity equation for the CSF flow in the SAS without choroid plexus interaction is

$$\frac{\partial\{A_j[h_j + y_j(t)]\}}{\partial t} = q_{j-1} - q_{e,j}, \quad j \in \{\mathrm{SAS}\}. \quad (5)$$

Diffusive reabsorption of CSF $q_{e,j}$ occurs in SAS according to

$$q_{e,j} = \kappa\left[p_j(t) - p_0(t)\right], \quad j \in \{\mathrm{SAS}\}. \quad (6)$$

CSF produced by the choroid plexus is assumed not to seep into the parenchyma under normal circumstances [25]. The periventricular tissue lining all ventricles is modeled by linear elastic springs. The SAS is between the cortical surface and the cranium. Its expansion is more restricted due to the tethering arachnoid strands (trabeculae). We have modeled this higher elastance with a stronger elasticity constant. In effect, the SAS is harder to expand than the ventricles in our model.

TABLE I
TISSUE AND FLUID PROPERTIES

Property	Value	Source
Young Modulus for ventricles	2,100 N/m^2	[27]
Young Modulus for SAS	3,500 N/m^2	Derived from [28]
Fluid density, ρ_f	1,004 - 1,007 kg/m^3	[29]
Fluid viscosity, μ	10^{-3} Pa s	i.e. water
Spring elasticity, k_e	8 N/m (normal)	Extracted
Brain Dampening , k_d	0.35×10^{-3} (N s)/m	Assumed - low dampening effect
Ependyma density, ρ_w	1,000 kg/m^3	i.e. water
Reabsorption constant, κ	1.067×10^{-11} m^3/(Pa s)	Estimated

The simplified equations of motion for the hydrodynamics of the 1-D intracranial dynamics are summarized in (2)–(6). The forces acting on the ventricular wall include the pressure difference between the tissue and the fluid $(p_i(t) - p_0)$, the elastic tissue compliance $(k_e y_i(t))$ and dissipation by a first-order dampening force $(k_d\dot{y}_i(t))$ (2). The continuity and momentum equations for the motion of the fluid are expressed in (3) and (4) and are equivalent to a finite volume flow discretization with staggered grid coupled with a thin linear elastic membrane. The reabsorption is modeled as diffusive mass transfer driven by pressure difference [see (6)].

The fluid-structure interaction equations constitute a differential algebraic equation system (DAE) of index two. The computational parameters include CSF and tissues' mechanical properties are listed in Table I. The inputs of the simulation are the CSF production rate, $q_{f,i}$, the choroid expansion, $a(t)$, and the venous blood pressure, $p_0(t)$. The choroid expansion and venous blood pressures are coupled with the heart beat. The simulation computes pressures in all the ventricles and the SAS, the flow velocities in the foramina (v_i), and the tissue deformation (y_i) at each point in time. The system was integrated using the standard DASSL solution algorithm [26]. All simulations were also validated by solving the identical equation set in the Laplace domain with the help of the Simulink package of Matlab [19].

IV. PREDICTIONS OF THE MODEL

The computations quantify the pulsatility of the CSF flow and ICP in a normal brain. The results also approximate the relevant velocities and pressures of the CSF in the ventricles in dynamic interaction with the linear elastic brain parenchyma.

We first consider the normal pulsations of lateral ventricles and CSF production. In the human, the choroid plexus produces CSF at a rate of 0.32 cm^3/min [29]. The amplitude of choroid expansion, $a(t)$, was deduced from medical literature [5], [29] and from published data about ventricular pulsation [6], [7], to be in the range of 1.29–1.55 cm^3/min at each cardiac cycle. The transient choroid expansions were modeled as a quasisinusoidal function with the same pattern and frequency as the arterial blood pressure, see (1). Fig. 7 shows the choroid expansion for a pulse rate of 1 Hz. The choroid expansion induces CSF motion and causes the elastic ventricles to expand. The ventricular movement is driven by the difference between the CSF ICP,

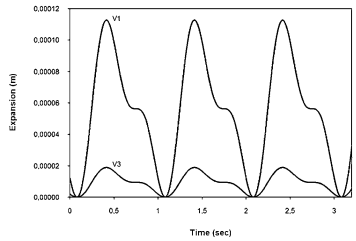

Fig. 7. Calculated expansion of the choroid plexus in the lateral (V1) and third ventricles (V3).

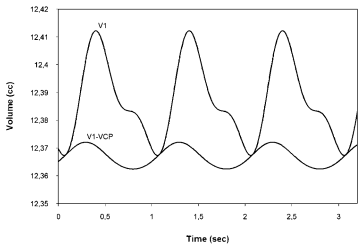

Fig. 8. The volume of the lateral ventricle (V1) versus the CSF content. The CSF content is the difference between the ventricular volume (V1) versus the expansion of the coroid plexus (VCP).

$p_i(t)$, and the brain tissue pressure, which is assumed to be at venous pressure levels, $p_0(t)$ ($\sim$10 mmHg).

The simulation shows that the largest tissue displacements and stresses occur in the lateral ventricles. Fig. 8 shows that the ventricles have the maximum volume in systole, while their fluid content is the smallest. The simulations indicate a 4.5% volume variation in the lateral ventricles in each cardiac cycle, corresponding to approximately 1 mm radius increment of an equivalent sphere. The volume variation is confirmed by the MRI measurement of Lee at al. [13], although the volume enlargement of 10%–20% they reported is higher than our prediction. The CSF production rate in the third and fourth ventricle (total of 0.032 cm^3/min) is small compared to the production rate in the lateral ventricles. The volume variations in the third and fourth ventricles are much smaller than the lateral ventricles also, only 0.6% and 0.5%, respectively. The pressure distributions were also computed for the entire ventricular system as depicted in Fig. 9. A slight lag in the pressure peak is also seen along the CSF pathways from V1 to V4 and then to SAS.

Clinical evidence shows that the CSF motion in the AS reverses with each cardiac cycle [5], [6]. How can flow reversal occur when CSF motion is driven by arterial and venous blood pressure difference, which is always positive? The schematic of Fig. 6 and the simulations of Figs. 7–10 help to resolve this puzzle. In each systole, the pulsations stretch the ventricles and SAS and, thus, elastic energy is stored. In effect, high systolic pressure loads the "springs" of the elastic parenchyma. In the diastole, the arteries relax, thus causing a choroid contraction. Since the choroid contraction in the diastole exceeds the recovery of elastic tissue strain of the ventricular wall, the fluid flow reverses. The cyclic expansion of observable outer dimensions of the ventricles versus its CSF content is depicted in Fig. 8. Note that this type of flow pattern can only occur in systems with distensible boundaries.

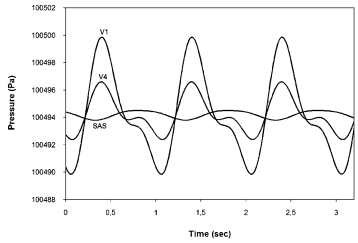

Fig. 9. The ICP along the ventricular pathways (pressure profile).

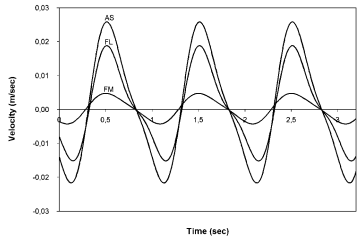

Fig. 10. Flow rates in the foramina of Monro, aqueductus and the foramina of Magendie.

TABLE II
SIMULATION RESULTS COMPARED WITH EXPERIMENTAL OR PUBLISHED PHYSIOLOGICAL DATA

Clinical Observation	Model Prediction	Literature Value
Ventricular enlargement	±4.5 %	5 - 20 % [13]
Velocity - Foramen of Monro	+4.7 / -4.3 mm/s	1 - 3 mm/s [7]
Velocity - Aqueduct of Sylvius	+25.8 / -21.7 mm/s	23 mm/s [23] 3.7 - 7.6 mm/s [7]
	average +1.5 mm/s	average +2 mm/s [5]
Velocity - Foramen of Luschke	+18.8 / -15.2 mm/s	2.4 - 5.6 mm/s [7] 50 mm/s, Foram. Magnum [5]
Velocity - Subarachnoid space	not computed	3 cm/s (CINE MRI) 5 cm/s, at Foram. Magnum [5]

The velocity plots in Fig. 10 show that the largest velocities occur in the AS with peak velocities of $+25.8$ mm/s and -21.7 mm/s, and averages of $+1.5$ mm/s. There is also a net forward CSF flow rate of $+0.3$ cm^3/min (the production rate in lateral and third ventricles). Observations with flow sensitive MRI demonstrated the same pulsating wave characteristic as depicted in the computational results of Fig. 10 [7]. The maximal velocities in the FM and FL in the model are 4.7 mm/s and 18.8 mm/s, respectively. The calculated results are compared with published physiological data in Table II.

The reabsorption of CSF occurs via the arachnoid villi in the SAS. Under normal conditions, CSF reabsorption is in equilibrium with CSF production. In a SAS without any obstruction, the pressure gradients are very low, so that diffusion-driven mass transfer flux according to (6) is basically distributed evenly along the sagittal sinus. The average pressure difference between the SAS and venous pressure was calculated to be 494 Pa; this number is in agreement with published literature values [30].

The expansion of the ventricular volume leads to an increase in ICP in accordance with the increased tissue compliance as prescribed by (2). The pressures in Fig. 9 show a peak ICP difference of approximately 10 Pa during the cardiac cycle. Our simulations are in good agreement with the dog experiments,

although the dog anatomy (such as the dimensions of ventricles and foramina) is different from that of the human brain. Our fluid dynamic computations offer a compelling explanation for the small pressure gradients. Large pressure gradients would require high Reynolds numbers or a different geometry (i.e., very narrow foramina). The large gradients along the normal flow direction can only build in the ventricular system with occluded proximal CSF pathways.

The ICP that drives the flow reversal must exhibit a sign change during each cardiac cycle. This suggests that large transmural pressure gradients cannot exist when the foramina are open. The pulsatile pattern of CSF flow and its magnitude is also an indirect proof of tissue compliance (arteries and parenchyma). Without compliant tissues, the flow can only be unidirectional, not reversible. For an approximately constant CSF volume (neglecting the small production), the incompressible CSF can only pulsate when the boundaries are elastically deforming.

V. Model Validation

The prediction of only small transmural pressure gradients constitutes a departure from existing hypotheses about the formation of hydrocephalus. In support of our novel proposition, the validation includes: 1) 2-D dynamic CFD simulations; 2) *in vivo* CINE phase-contrast imaging of CSF velocities in a normal human subject; and 3) a hydraulic experiment with a surrogate "hydraulic brain model."

A. Two-Dimensional CFD Simulation of the Ventricular Dynamics

The assumptions of the 1-D fluid-structure interaction model for pulsatile intracranial dynamics were validated using a rigorous 2-D CFD analysis. A high resolution computational grid with 5635 mesh faces was generated from a sagittal MR image of the ventricles and the foramina with image processing software. In the simulations using a commercial CFD code, boundary conditions along the choroid plexus were adjusted dynamically to model sinusoidal choroid expansion. The ventricular walls were, however, considered rigid due to the limitations of the CFD code [20]. The resulting pulsatile transient pressure and velocity fields were in good agreement with our fluid-interaction model. The CSF pressures in the diastole are depicted in Fig. 11 (right). The maximum pressure difference in the lateral ventricle was around 0.1 Pa and was less than 2 Pa in the whole domain. This outcome supports the earlier uniform pressures assumption for the ventricles. The averaging process of our 1-D model assumed parabolic radial velocity profiles in the foramina. The parabolic shape of the radial velocity was confirmed from this 2-D simulation, thus justifying the simplified assumptions discussed in the previous model. The velocity field at diastole, as shown in Fig. 11 (left), corroborates the location of velocity maxima in the AS. The maximum aqueduct velocity of the order of 7.3 mm/s is close to the values obtained with our 1-D fluid-structure interaction model. The detailed 2-D CFD analysis demonstrated the validity of the basic assumptions of the 1-D model of intracranial dynamics. A full dynamic analysis of the 3-D dynamic stress and strain state of the brain will be the objective of future work.

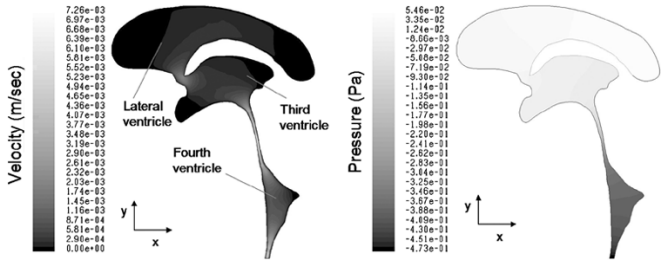

Fig. 11. The 2-D velocity (left) and pressure (right) contours in the ventricular space at half of the cardiac cycle.

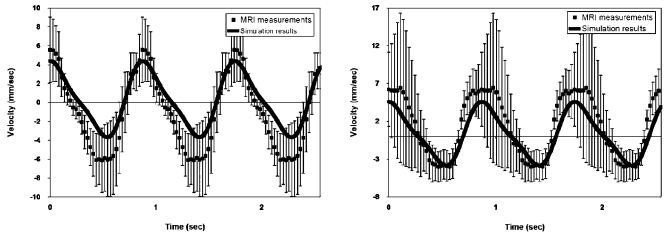

Fig. 12. Comparison of CSF flow velocities measured with CINE phase-contrast MR imaging versus. simulation results (a) at the third ventricle, and (b) at the region between the AS and the fourth ventricle.

B. Validation of CSF Flow Velocities With MRI

Our proposed model was further validated by *in vivo* CSF flow velocity measurements with CINE phase-contrast MRI. The phase-contrast technique is based on the fact that transverse magnetization of moving spins accumulates a different phase than static spins in the presence of a magnetic field gradient. This different phase accumulation can be applied to quantify the flow velocities [31]. CINE (or time resolved) MRI collects images at multiple points of the cardiac cycle with data acquisition triggered by cardiac gating. The data are acquired through multiple cardiac cycles and the final results are computed by linear interpolation. A 2-D CINE phase-contrast technique was applied to collect CSF flow data from the brain of a 52-year old healthy male on a 3 Tesla GE Signa scanner (GE Medical Systems, Milwaukee, WI) equipped with a standard quadrature bird-cage head coil. Cine phase-contrast images at 32 equal-increment time points of the cardiac cycle were first collected from a coronal slice located at the middle of the third ventricle and then were collected from an axial slice located between the AS and the fourth ventricle. Only the velocity perpendicular to the slice of interest was measured. A maximum velocity (VENC) of 5 cm/s was chosen as the limit, so that a reasonable velocity resolution could be achieved for CSF flow measurement. The velocity at each pixel location was corrected through basic subtraction by the time-average "velocity" of a nearby solid brain tissue "background" [8], [9], [32]. The regions of interest (ROIs) were drawn to include all the CSF areas at the third ventricle for one slice and then at the region between the AS and the fourth ventricle for the other slice. The mean velocity and standard deviation were calculated at each ROI.

Fig. 12 displays the mean velocity and its standard deviation at two different ROIs in three cardiac cycles. The velocity data clearly show the forward-reverse oscillatory motion of the CSF

at both regions. This flow pattern is in excellent agreement with our simulations. The measured mean and maximum oscillatory velocities across the ROI at the third ventricle were 3.6 mm/s and 6.1 mm/s, respectively. Those at the region between the AS and the fourth ventricle were 3.9 mm/s and 6.4 mm/s, respectively. Although not measured exactly inside the AS, these numbers are within the range reported in the literature [7]. We also observed the slow oscillatory motion of the brain parenchyma as reported by Enzmann *et al.*, who have claimed that compliant brain tissues appear to be the driving force for CSF pulsation [9]. Simulation results were obtained with our 1-D pulsatile CSF flow model. For precision in the comparison of the measured and computed velocity vectors in Fig. 12, the cross sectional areas of the computational section were set equal to the ROI in the MR measurement. Thus, the model and the human subject data were in close agreement.

C. Experiments Using a "Hydraulic" Model Brain

After removal of the choroid plexus in one lateral ventricle and kaolin injection, Bering observed one-sided ventricular enlargements in dogs [14]. With open foramina of Monro, both lateral ventricles are exposed to the same pressure differences between the lateral ventricles and the SAS. Hence, despite the choroid plexectomy, both ventricles should experience the same transmural pressure differences and should expand equally. However, Bering found that only the ventricle with an intact choroid plexus increased in size. Animal experiments by Wilson [16] and Di Rocco [17], [18] produced similar findings. Asymmetric hydrocephalus found in these experiments cannot be explained by any existing theory. It appears to hold the key to fully understand the role of ICP. If large transmural pressures gradients were responsible for communicating hydrocephalus, then it is baffling why the removal of the choroid plexus on one side, as Bering did, would prevent its formation. High transmural pressure differences appear to be at odds with the experimental evidence.

We conducted a set of simple hydraulic experiments to explain asymmetrical expansion of lateral ventricles [33]. The apparatus depicted in Fig. 13 behaves similar to the modeled brain dynamics. A simple water-filled tank represents the cranial cavity and the brain parenchyma. Two rubber balloons stand for the lateral ventricles enclosed by elastic periventricular cells. The CSF is modeled by water inside the balloons. The brain parenchyma's compliance corresponds to the rubber's elastic properties; its bulk is analogous to the water in the tank. The two "ventricular" balloons were connected with a small T-piece and 2 mm diameter plastic tubes emulating the foramina of Monro. The SAS was modeled by a flexible rubber hose connected to the ventricles on one side and atmosphere at the loose end.

The ventricular balloons could be pulsated from within by two flexible rubber balloons of a smaller size representing the choroid plexus. The blood supply to the choroid plexus was emulated by forcing compressed air into the inner balloons. When air was pressed through the "choroid" balloons as described above, CSF motion was induced in both ventricles and the balloons started to oscillate with periodic displacement of

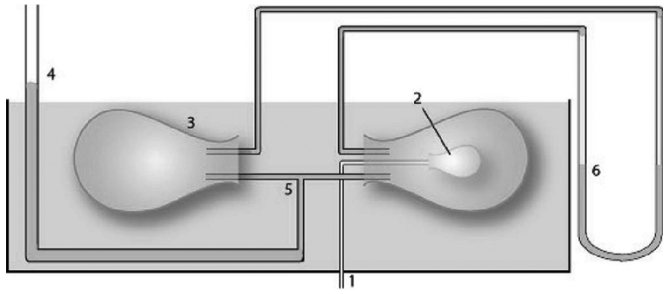

Fig. 13. The balloon experiment design (1. choroid artery, 2. choroid plexus, 3. lateral ventricle, 4. SAS, 5. Foramen, 6. water-oil udometer). Only one of the two choroidal balloons is shown.

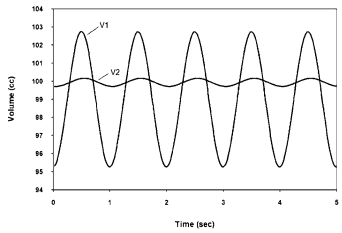

Fig. 14. Selective large expansion of ventricular balloon V1 (with intact choroid plexus). Ventricular balloon V2 (without choroid plexus) oscillates with lower amplitude.

the "water parenchyma." The magnitude of the ventricular expansion was estimated by counting the pixels of digital images obtained by a high-resolution video camera. A water-oil udometer measured the pressure differences between the "ventricular" balloons.

By stopping the air supply to only one of the ventricular balloons, we emulated the effect of unilateral choroid plexectomy of Bering's dog experiments. We observed that only the "ventricle" with intact "choroid plexus" exhibited large expansion. The second ventricular balloon was also pulsating, but with much smaller amplitude as can be seen in Fig. 14. The mean pressure difference between the two ventricular balloons did not exceed 10–15 mm water ($\sim$100–150 Pa), yet only one "ventricle" enlarged significantly. This large amplitude oscillation causes larger strains and stresses on one side, while the other side experiences relatively lower stresses. Hence, we found a wide gap in the ICP amplitudes, while the mean pressures were similar as in the case of Bering's experiment. Larger ICP amplitudes cause strong tissue stresses on one side, eventually leading to asymmetric ventricular expansion. This asymmetric ventricular expansion was observed experimentally without any "transmural" pressure difference between the "ventricles" and "water parenchyma." The total pressure in the "subarachnoid" space did not exceed 600 Pa [33].

Computer simulation for the hydraulic brain model using Young's Modulus of rubber and the dimensions of the tank experiment are in good agreement with each other. Fig. 14 depicts the computed amplitudes of volumetric expansion of 7.47 cm^3 for the intact ventricle and only 0.45 cm^3 for the ventricle with choroid oblation. The predicted pressure differences are displayed in Fig. 15 and compare well with the experimental values of 100–160 Pa. These experiments and the mathematical interpretation of our model provide to the best

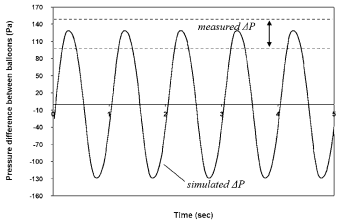

Fig. 15. The pressure between the two simulated ventricular balloons.

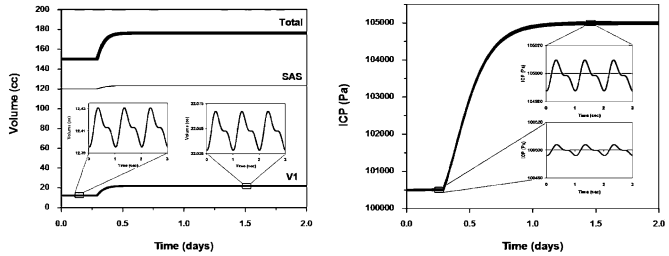

Fig. 16. Simulation of ventricular enlargement and ICP increase during the formation of acute hydrocephalus.

of the authors' knowledge the first plausible explanation for Bering's asymmetric hydrocephalus.

We also extrapolated our computations beyond normal conditions in order to simulate the onset of acute hydrocephalus as experienced by one of our dogs. We reduced the CSF reabsorption constant, κ, to reflect the decreased absorption after kaolin injection. Indeed, the model predicted large ventricular expansions and an increase in ICP as depicted in Fig. 16. These results compare well with the acute ICP data obtained with the INSITE pressure measurements of Figs. 2 and 3. A detailed analysis of hydrocephalus in acute and chronic form as well as its models for existing therapeutic options will be the subject of a follow-up paper.

VI. Conclusion

A series of dog experiments provided the impetus to create a new model of ICP and CSF flow dynamics. Large transmural pressure gradients were not found in animals with communicating hydrocephalus induced by kaolin injection. Based on these experiments, a comprehensive fluid-mechanical model for the pulsatile cerebral spinal fluid (CSF) flow in the brain was developed.

Our fluid-structure interaction model developed from first principles rendered predictions for pressure and velocity distributions which were in good agreement with animal and human data. The pulsatile motion of the cerebrospinal flow was linked to arterial blood flow in the choroid plexus. Under normal conditions, CSF production and reabsorption flux are in equilibrium leading to ventricular size variation of a few percent, but no average size increase. A breakdown of CSF reabsorption can cause CSF accumulation leading to expanded ventricles. The model also clarifies the role of ICP rise during the formation of communicating hydrocephalus. The rise is not a cause of hydrocephalus, but an effect of increased fluid due to lowered absorption of CSF. For the first time, the new pulsatile hypothesis offers a plausible explanation for the formation of asymmetric hydrocephalus. The pulsatile velocity fields agree qualitatively with the measurements from our CINE phase-contrast MRI experiment.

More complex distribution patterns of the arterial pulsations are probably the cause of bi-directional flows observed in the fourth ventricle and the prepontine/cervical SASs [9], [11]. It would be interesting to incorporate the actual timing of the arterial pressure waves into the forcing functions $a(t)$. The timing of the pressure waves from data in the literature [6], [9], [11] is easily incorporated into the model by substituting the corresponding timing of the pulse wave into the external forcing function of the ventricles. That discussion is, however, beyond the scope of this paper.

In future work, we plan to study more complex CSF patterns such as bi-directional flow in the fourth ventricle by studying the precise timing of the arterial pressure waves entering the cranium. Our model also provides the fundamental mathematical relations necessary for eventually building a detailed 3-D stress-strain analysis of the brain with dynamic fluid-structure interaction. The extension of this work will also show options for devising novel treatment options that might improve the prognosis of patients with hydrocephalus.

References

[1] S. Hakim, J. G. Venegas, and J. D. Burton, "The physics of the cranial cavity, hydrocephalus and normal pressure hydrocephalus: Mechanical interpretation and mathematical model," *Surg. Neurol.*, vol. 5, pp. 187–210, 1976.

[2] R. D. Penn, M. C. Lee, A. A. Linninger, K. Miesel, S. N. Lu, and L. Stylos, "Pressure gradients in the brain: An experimental model of hydrocephalus," *J. Neurosurg.*, May 2005, to be published.

[3] M. D. F. Deck, V. Deonarine, and D. G. Potts, "The rate of cerebrospinal fluid formation proximal and distal to aqueductal obstruction in the dogs," *Neuroradiology*, vol. 108, pp. 607–611, 1973.

[4] M. J. Johnson, I. Ayzman, A. S. Wood, J. A. Tkach, J. Klauschie, D. J. Skarupa, J. P. McAllister, and M. G. Luciano, "Development and characterization of an adult model of obstructive hydrocephalus," *J. Neurosci. Meth.*, vol. 91, pp. 55–65, 1999.

[5] M. Egnor, L. Zheng, A. Rosiello, F. Gutman, and R. Davis, "A model of pulsations in communicating hydrocephalus," *Pediatr. Neurosurg.*, vol. 36, pp. 281–303, 2002.

[6] D. Greitz, "Cerebrospinal-fluid circulation and associated intracranial dynamics. A radiologic investigation using MR-imaging and radionuclide cisternography," *Acta. Radiol.*, vol. Suppl. 386, pp. 1–23, 1993.

[7] T. P. Naidich, N. R. Altman, and S. M. Gonzalez-Arias, "Phase contrast cine magnetic resonance imaging: Normal cerebrospinal fluid oscillation and applications to hydrocephalus," *Neurosurg. Clin. N. Am.*, vol. 4, no. 4, pp. 677–705, 1993. Review.

[8] N. Alperin, E. M. Vikingstad, B. Gomez-Anson, and D. N. Levin, "Hemodynamically independent analysis of cerebrospinal fluid and brain motion observed with dynamic phase contrast MRI," *Magn. Reson. Med.*, vol. 35, no. 5, pp. 741–754, 1996.

[9] D. R. Enzmann and N. J. Pelc, "Brain motion: Measurement with phase-contrast MR imaging," *Radiology*, vol. 185, no. 3, pp. 653–660, 1992.

[10] J. E. A. O'Connell, "The vascular factor in intracranial pressure and the maintenance of the cerebrospinal fluid circulation," *Brain*, vol. 66, pp. 204–228, 1943.

[11] D. R. Enzmann and N. J. Pelc, "Normal flow patterns of intracranial and spinal cerebrospinal fluid defined with phase-contrast cine MR imaging," *Radiology*, vol. 178, no. 2, pp. 467–474, 1991.

[12] G. H. Du Boulay, "Pulastile movement in the CSF pathways," *Br. J. Radiol.*, vol. 39, pp. 255–262, 1966.

[13] E. Lee, J. Wang, and R. Mezrich, "Variation of lateral ventricular volume during the cardiac cycle observed by MR imaging," *Am. J. Neuroradiol.*, vol. 10, pp. 1145–1149, 1989.

[14] E. A. Bering, "Circulation of the cerebrospinal fluid: Demonstration of the choroid plexuses as the generator of the force for flow of fluid and ventricular enlargement.," *J. Neurosurg.*, vol. 19, pp. 405–413, 1962.

[15] W. E. Dandy, "Experimental hydrocephalus," *Ann. Surg.*, vol. 70, pp. 129–142, 1919.

[16] C. B. Wilson and V. Bertan, "Interruption of the anterior choroidal artery in experimental hydrocephalus," *Arch. Neurol.*, vol. 17, pp. 614–619, 1967.
[17] V. E. Pettorossi, C. Di Rocco, R. Mancinelli, M. Caldarelli, and F. Velardi, "Communicating hydrocephalus induced by mechanically increased amplitude of the intraventricular cerebrospinal fluid pulse pressure: Rationale and method," *Exp. Neurol.*, vol. 59, pp. 30–39, 1978.
[18] C. Di Rocco, V. E. Pettorossi, M. Caldarelli, R. Mancinelli, and F. Velardi, "Communicating hydrocephalus induced by mechanically increased amplitude of the intraventricular cerebrospinal fluid pressure: Experimental studies," *Exp. Neurol.*, vol. 59, pp. 40–52, 1978.
[19] A. A. Linninger, C. Tsakiris, A. Munoz, M. Lee, and R. Penn, "Hydrodynamics of the cerebrospinal fluid flow in the human brain," presented at the AIChE Annual Meeting, San Francisco, CA, Nov. 16–Nov. 21 2003. Paper 462g.
[20] Fluent, Inc., Lebanon, NH.. [Online]. Available: http://fluent.com/software/
[21] B. S. Brooks, S. A. E. G. Falle, and T. J. Pedley, "Numerical Solutions for unsteady gravity-driven flows in collapsible tubes: Evolution and roll-wave instability of a steady state," *J. Fluid Mech.*, vol. 396, pp. 223–256, 1999.
[22] S. V. Pantakar, "Numerical heat transfer and fluid flow," in *Computational Methods in Mechanics and Thermal Sciences*, W. J. Minkowycz and E. M. Sparrow, Eds. New York: McGraw-Hill, 1980, pp. 84–85.
[23] E. E. Jacobson, D. F. Fletcher, M. K. Morgan, and I. H. Johnston, "Fluid dynamics of the cerebral aqueduct," *Pediatr. Neurosurg.*, vol. 24, pp. 229–236, 1996.
[24] M. Zagzoule and J.-P. Marc-Vergnes, "A global mathematical model of the cerebral circulation in man," *J. Biomechanics*, vol. 19, no. 12, pp. 1015–1022, 1986.
[25] D. N. Levine, "The pathogenesis of normal pressure hydrocephalus: A theoretical analysis," *Bull. Math. Biol.*, vol. 61, pp. 875–916, 1999.
[26] K. E. Brenan, S. L. Campbell, and L. R. Petzold, *Numerical Solution of Initial Value Problems in Differential Algebraic Equations*. Philadelphia, PA: SIAM, 1996.
[27] M. I. Miga, K. D. Paulsen, P. J. Hoopes, F. E. Kennedy, A. Hartov, and D. W. Roberts, "*In vivo* modeling of interstitial pressure in the brain under surgical load using finite elements," *Trans. ASME/J. Biomechan. Eng.*, vol. 122, pp. 354–363, 2000.
[28] P. Aimedieu and R. Grabe, "Tensile strength of cranial pia mater: Preliminary results," *J. Neurosurg.*, vol. 100, pp. 111–114, 2004.
[29] J. E. Bruni, "Cerebral ventricular system and cerebrospinal fluid," *Encyclopedia of Human Biology*, pp. 635–643, 1977.
[30] K. Shulman and J. Ransohoff, "Sagittal sinus venous pressure in hydrocephalus," *J. Neurosug.*, vol. 23, pp. 169–173, 1965.
[31] C. L. Dumoulin, S. P. Souza, M. F. Walker, and E. Yoshitome, "Time-resolved magnetic-resonance angiography," *Magn. Reson. Med.*, vol. 6, no. 3, pp. 275–286, 1988.
[32] M. H. Buonocore and H. Bogren, "Factors influencing the accuracy and precision of velocity-encoded phase imaging," *Magn. Reson. Med.*, vol. 26, no. 1, pp. 141–154, 1992.
[33] Z. Danziger and A. Linninger. (2003, Aug.) Modeling cerebral blood flow and pressure in elastic tubes using a finite element approach: Its relation to symptoms in hydrocephalus. Laboratory for Product and Process Design (LPPD), Chicago, IL. [Online]. Available: http://vienna.che.uic.edu/Laboratory/laboratory.htm

Andreas A. Linninger received the Ph.D. degree from the Vienna University of Technology, Vienna, Austria.

He is an Associate Professor in the Departments of Chemical Engineering and Computer Science at the University of Illinois at Chicago, Chicago. His research interests include hydrocephalus, computational models for intracranial dynamics, and drug delivery to the human brain.

Cristian Tsakiris received the Ph.D. degree from Politehnica University, Bucharest, Romania, in 2000.

He is a Postdoctoral Research Associates with the Laboratory for Product and Process Design, Department of Chemical Engineering, University of Illinois at Chicago, Chicago. His research interests are in computational fluid dynamics and transport phenomena.

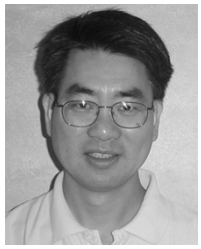

David C. Zhu received his Ph.D. degree from the University of California at Davis. He is a Research Associate (Assistant Professor) of Radiology at the University of Chicago. His main research interests concern magnetic resonance imaging and biomedical engineering.

Michalis Xenos received the M.S. and Ph.D. degrees from the University of Patras, Patras, Greece, in 2003.

He is a Postdoctoral Research Associates with the Laboratory for Product and Process Design, Department of Chemical Engineering, University of Illinois at Chicago, Chicago. His research interests are in computational fluid dynamics and transport phenomena.

Peter Roycewicz received the B.S. degree from University of Illinois at Chicago, Chicago, in 2004.

He contributed to this paper during an NSF-sponsored summer research experience for undergraduate students.

Zachary Danziger received the B.S. degree from University of Michigan, Ann Arbor, in 2004.

He contributed to this paper during an NSF-sponsored summer research experience for undergraduate students.

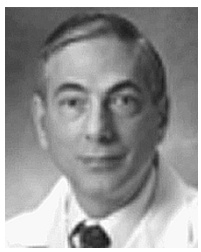

Richard D. Penn received M.D. degree from Columbia University College of Physicians and Surgeons. He is a Professor in the Department of Neurosurgery at the University of Chicago. His main research interests are hydrocephalus and drug delivery to the brain.